https://doi.org/10.3847/1538-4357/ab52fd

Exploring the Grain Properties in the Disk of HL Tau with an Evolutionary Model

Carlos Tapia[1] , Susana Lizano[1] , Anibal Sierra[1] , Carlos Carrasco-González[1] , and Elly Bayona-Bobadilla[1,2]
[1] Instituto de Radioastronomía y Astrofísica, Universidad Nacional Autónoma de México, Apartado Postal 3-72, C.P. 58089 Morelia, Michoacán, México
[2] Instituto de Ciencias Nucleares, Universidad Nacional Autónoma de México, Apartado Postal 70-468, C.P. 04510 Cd. Mx., México

Abstract

We model the ALMA and Very Large Array (VLA) millimeter radial profiles of the disk around HL Tau to constrain the properties of the dust grains. We adopt the disk evolutionary models of Lynden-Bell & Pringle and calculate their temperature and density structure and emission. These disks are heated by the internal viscosity and irradiated by the central star and a warm envelope. We consider a dust size distribution $n(a)\,da \propto a^{-3.5}\,da$, and vary the maximum grain size in the atmosphere and the midplane, $a_{\max} = 100\,\mu$m, 1 mm, and 1 cm. We also include dust settling and vary the dust-to-gas mass ratio from 1 to 9 times the ISM value. We find that the models that can fit the observed level of emission along the profiles at all wavelengths have an atmosphere with a maximum grain size $a_{\max} = 100\,\mu$m, and a midplane with $a_{\max} = 1$ cm. The disk substructure, with a deficit of emission in the gaps, can be due to dust properties in these regions that are different from those in the rings. We test an opacity effect (different $a_{\max}$) and a dust mass deficit (smaller dust-to-gas mass ratio) in the gaps. We find that the emission profiles are better reproduced by models with a dust deficit in the gaps, although a combined effect is also possible. These models have a global dust-to-gas mass ratio twice the ISM value, needed to reach the level of emission of the 7.8 mm VLA profile.

Unified Astronomy Thesaurus concepts: Stellar accretion disks (1579); Protoplanetary disks (1300); Young stellar objects (1834); T Tauri stars (1681); Radiative transfer equation (1336)

1. Introduction

The HL Tau disk was one of the first sources where a high angular resolution map revealed a disk with multiple rings and gaps (ALMA Partnership et al. 2015). Many physical models have been proposed to explain the structure observed in this disk, these include planets in the gaps (Jin et al. 2016), three planets and disk evolution (Dipierro et al. 2015), a super-Earth and a low viscosity disk (Dong et al. 2018), dust radial migration and ice lines (Okuzumi & Tazaki 2019), and gaps at the edge of the disk dead zone (Flock et al. 2015). In addition, several other papers have inferred dust physical properties (maximum grain size, dust temperature, and optical depth) by modeling the observed multiwavelength emission either by fitting the disk parameters or by calculating the structure of passive disks irradiated by the central star (e.g., Kwon et al. 2015; Carrasco-González et al. 2016; Pinte et al. 2016; Liu et al. 2017; Carrasco-González et al. 2019, hereafter CG19). All these latter investigations infer millimeter dust grains in the HL Tau disk based on the observed small spectral indices. These millimeter values differ from the maximum grain size of some hundreds of micrometers required to explain the observed dust polarized emission (e.g., Kataoka et al. 2015, 2017). It is not clear yet what is causing the disagreement between the estimates of the dust grain sizes. One possibility is that the polarized emission observed at ALMA wavelengths is mainly tracing the dust grains in the disk atmosphere, while the longer VLA wavelengths trace deeper regions of the disk, closer to the midplane, where larger grains are expected to lie due to dust settling. Another possibility is a different dust composition as discussed recently by Yang & Li (2019) who found that dust grains of absorptive carbonaceous material and a distribution with a maximum grain size of 3 mm can produce both the observed level of polarization and small spectral indices. It is therefore important to study the emission of disks with different

dust properties and compare with multiwavelength observations, to improve our understanding of their physical properties.

Knowledge of the dust physical properties and their evolution is fundamental to explain the structure of the disks observed at millimeter wavelengths. Recently, ALMA high angular resolution observations of 20 nearby protoplanetary disks in the DSHARP project exposed the prevalence of different morphologies and substructure such as vortices, spiral arms, and rings (Andrews et al. 2018). Hopefully, in the near future one will be able to obtain high angular resolution multiwavelength information of all these sources in order to obtain detailed diagnostics of the dust properties in these disks.

In this work, we study the HL Tau disk using the viscously evolving disk models of Lynden-Bell & Pringle (1974) with the age of the HL Tau system. We calculate the emission of these disks with different dust properties and compare it with the observed millimeter emission. To do this we calculate the radial and vertical structure of these models heated by the internal viscosity, and irradiated by both the central source and a warm envelope (Lizano et al. 2016; Tapia & Lizano 2017). We then compare the azimuthally averaged intensity profiles of the models with four observed ALMA and VLA millimeter profiles in order to constrain the physical properties of the dust in the disk.

This paper is organized as follows: Section 2 briefly describes the Lynden-Bell & Pringle evolutionary disk models. Section 3 explains how the dust settling is included in these models. Section 4 summarizes the star and disk parameters of the fiducial model, while Section 5 describes the observed millimeter profiles. In Section 6 we obtain the emission of the models at millimeter wavelengths, to find the dust properties that can produce the observed level of emission along the profiles. Next, in Section 7, we explore the effect of changing the dust properties in the gaps in order to reproduce the observed bright-dark ring substructure of the HL Tau disk. In

Section 8 we discuss the effect of changing the parameters of the fiducial model: the dust settling parameters, the initial disk mass, and the initial accretion rate. The discussion and conclusions are presented in Sections 9 and 10, respectively.

2. Evolutionary Disk Model

The radial structure of viscously evolving accretion disks with a power-law viscosity, $\nu \propto R^\gamma$, was found by Lynden-Bell & Pringle (1974). Due to the viscous evolution, the disk surface density and mass accretion rate decrease with time. Here we will study models with a viscosity exponent $\gamma = 1$ which can fit the decline of the mass accretion rate with time for T Tauri stars with different ages (Hartmann et al. 1998; Manzo-Martínez et al. 2019, in preparation). Following the normalization of Hartmann et al. (1998) the viscosity can be written as

$$\nu = \nu_1 \left(\frac{R}{R_1} \right), \tag{1}$$

where R_1 is a normalization radius, and ν_1 is the viscosity at R_1. The gas surface density is a power law with an exponential cutoff given by

$$\Sigma(R, \mathbb{T}) = \frac{M_{d0}}{2\pi R_1^2} \left(\frac{R_1}{R} \right) \mathbb{T}^{-3/2} \exp\left(\frac{-R/R_1}{\mathbb{T}} \right), \tag{2}$$

and the disk mass is given by

$$M_d(R, \mathbb{T}) = \frac{M_{d0}}{\mathbb{T}^{1/2}} \left[1 - \exp\left(\frac{-R/R_1}{\mathbb{T}} \right) \right], \tag{3}$$

where M_{d0} is called the initial mass of the disk,[3] and the normalized time is

$$\mathbb{T} = \frac{t}{t_\nu} + 1, \tag{4}$$

where the viscous time is $t_\nu = R_1^2/(3\nu_1)$. In addition, the mass accretion rate is given by

$$\dot{M}_d(R, \mathbb{T}) = \frac{\dot{M}_{*0}}{\mathbb{T}^{3/2}} \exp\left(\frac{-R/R_1}{\mathbb{T}} \right) \left[1 - \frac{2R/R_1}{\mathbb{T}} \right], \tag{5}$$

where the initial mass accretion rate at the center is

$$\dot{M}_{*0} \equiv \frac{M_{d0}}{2t_\nu}. \tag{6}$$

For a disk with a given age $t = t_{age}$, the normalized time (Equation (4)) can be written as

$$\mathbb{T} = \frac{t_{age}}{t_\nu} + 1 = 2t_{age} \left(\frac{\dot{M}_{*0}}{M_{d0}} \right) + 1. \tag{7}$$

In addition, one can define a characteristic radius

$$R_c = R_1 \mathbb{T}, \tag{8}$$

where the exponential term in the surface density starts to dominate (see Equation (2)).

---

[3] Note that, for a finite disk with radius R_d, the initial disk mass is $M(R_d, 0) = M_{d0}\{1 - \exp(-R_d/R_1)\}$.

In terms of the normalized radius $r = R/R_c$, the gas surface density can be written as

$$\Sigma(r, \mathbb{T}) = \frac{M_{d0}}{2\pi R_c^2} \mathbb{T}^{-1/2} r^{-1} \exp(-r), \tag{9}$$

and using Equation (6), the viscosity in Equation (1) can be written as

$$\nu(r) = \frac{R_1^2}{3t_\nu} \left(\frac{R}{R_1} \right) = \frac{2}{3} \frac{\dot{M}_{*0} R_c^2}{M_{d0}} \mathbb{T}^{-1} r. \tag{10}$$

Given the age of the source t_{age}, the surface density and viscosity depend only on the initial disk mass M_{d0}, the initial mass accretion rate at the center $\dot{M}_{*0}$, and the characteristic radius R_c. These two functions are needed to determine the disk vertical structure and emission.

3. Dust-to-gas Mass Ratio and Dust Settling

The dust-to-gas mass ratio ζ will be described in terms of the dust ratio $\epsilon = \zeta/\zeta_{ISM}$, where $\zeta_{ISM} = 1/100$ is the ISM value. The dust and gas masses in protoplanetary disks can be obtained from millimeter continuum emission and CO isotopologue lines, respectively. Recently, Ansdell et al. (2016) made a survey of the dust and gas content of young protoplanetary disks in the Lupus star-forming region with ALMA. The lower panel of their Figure 3 shows the gas-to-dust mass ratio for the whole sample. The observed ratios correspond to values of the dust ratio $\epsilon \sim 0.1$–10. Also, Wu et al. (2018) studied the gas and dust content of the disk and envelope of HL Tau with lower resolution SMA observations. Since they do not resolve the disk, they modeled the continuum, ^{13}CO, and $C^{18}O$ observations. They estimate very low values of the disk gas-to-dust mass ratio, in the range 0.07–4, which corresponds to $\epsilon \sim 25$–1400 (see their Table 5, where they also summarize the results for other sources). It would be important to estimate the gas and dust content of HL Tau with high angular resolution studies to confirm these results. In this work, we will consider $\epsilon \geqslant 1$ as a model parameter to fit the observed ALMA and VLA dust continuum emission.

We also include the process of dust settling and grain growth in the disk models. Following D'Alessio et al. (2006), the disk has two regions: the atmosphere with small grains, and the midplane with bigger grains. We assume a dust grain size distribution given by $n(a)\,da \propto a^{-3.5}\,da$ (Mathis et al. 1977) with a minimum grain size $a_{min} = 0.005\,\mu m$, and vary the maximum grain size a_{max}, with different values of a_{max} for the grain population in the atmosphere and in the midplane. At each radius, the disk has a total dust mass determined by the dust-to-gas mass ratio $\zeta(R)$. This radial function can be used to take into account, for example, dust migration, growth, and sintering (e.g., Brauer et al. 2008; Okuzumi et al. 2016). One assumes for the atmosphere a dust-to-gas mass ratio ζ_{small} that takes into account the dust mass lost by settling to the midplane. The midplane has a dust-to-gas mass ratio ζ_{big} that takes into account the dust mass gained from the atmosphere. The surface density of the midplane is defined as $\Sigma_{big} = 2 \int_0^{z_{big}} \rho dz$ where z_{big} is the height of the midplane region and ρ is the gas volume density. The degree of dust settling is determined by the dust ratio $\epsilon_{small} = \zeta_{small}/\zeta_{ISM}$. Given the parameters ϵ_{small} and Σ_{big}, the Appendix shows the derivation of dust ratio in the midplane $\epsilon_{big} = \zeta_{big}/\zeta_{ISM}$.

Table 1
HL Tau Stellar and Disk Parameters

M_*[a]	age[b]	T_*[c]	R_*[c]	M_{d0}[d]	$\dot{M}_{*0}$[e]	R_d[f]	R_c[g]
$(M_\odot)$	(Myr)	(K)	$(R_\odot)$	$(M_\odot)$	$(M_\odot\ yr^{-1})$	(au)	(au)
1.7	1	4615	3.2	0.55	5×10^{-7}	150	80

Notes.
[a] Pinte et al. (2016).
[b] van der Marel et al. (2019).
[c] From Siess et al. (2000) evolutionary tracks of low and intermediate mass stars.
[d] Maximum stable disk mass.
[e] Initial mass accretion rate that corresponds to the measured mass accretion rate of HL Tau by White & Hillenbrand (2004).
[f] Pinte et al. (2016).
[g] Kwon et al. (2011).

4. Parameters of the Star–Disk Model

The values of the stellar and disk parameters of HL Tau are shown in Table 1: the stellar mass, age, temperature, and radius, the initial disk mass and mass accretion rate, the disk radius, and the characteristic radius. For the initial disk mass we choose $M_{d0} = 0.55 M_\odot$, less than the upper mass limit for disk stability, $M_d^{max} \sim M_*/3$ (Shu et al. 1990). The initial mass accretion rate $\dot{M}_{*0} = 5 \times 10^{-7} M_\odot\ yr^{-1}$ was obtained from Equations (5) and (7), given the actual mass accretion rate of HL Tau $\dot{M}_* = 10^{-7} M_\odot\ yr^{-1}$ measured by White & Hillenbrand (2004). The central luminosity is the stellar plus accretion luminosities, $L_c = L_* + \eta(GM_*\dot{M}_*)/R_*$, where the factor $\eta = (1 - R_*/R_{int})$ takes into account the disk truncation by the stellar magnetosphere and $R_{int} \sim 5R_*$ (Gullbring et al. 1998). For the parameters in Table 1, $L_c = 10.7 L_\odot$, which is within the luminosity range inferred by Robitaille et al. (2007) from the spectral energy distribution (SED) modeling of HL Tau. We will assume a distance to the HL Tau of 147 pc (Galli et al. 2018).

We first analyze a disk model with the parameters shown in this table. This model has the maximum gas surface density to be able to reproduce the level of the 7.8 mm VLA profile (see Section 5). The current mass of the disk is $M_d(R_d, 1\ Myr) = 0.28 M_\odot$ (see Equation (3)). We further assume that the dust is settled in the midplane with a dust ratio in the disk atmosphere $\epsilon_{small} = 0.1$ and a normalized gas surface density of the midplane $s_{big} = \Sigma_{big}/\Sigma(r, \mathbb{T}) = 0.4$; where $\Sigma(r, \mathbb{T})$ is given by Equation (9). For an isothermal disk, $s_{big} = 0.4$ corresponds to a settling height $z_{big} = 0.53\ H$, where H is the gas scale height evaluated at the midplane temperature (see the Appendix). We call the model with the parameters in Table 1 and the dust settling parameters $\epsilon_{small} = 0.1$ and $s_{big} = 0.4$, the *fiducial model*. Below we will explore the effect of varying these parameters with respect to the fiducial model.

For the dust composition, we assume a dust mixture of silicates, organics, and ice with mass fractional abundances with respect to gas $\zeta_{sil} = 3.4 \times 10^{-3}$, $\zeta_{org} = 4.1 \times 10^{-3}$, and $\zeta_{ice} = 5.6 \times 10^{-3}$, with bulk densities $\rho_{sil} = 3.3\ g\ cm^{-3}$, $\rho_{org} = 1.5\ g\ cm^{-3}$, and $\rho_{ice} = 0.92\ g\ cm^{-3}$ (Pollack et al. 1994). We use the code of D'Alessio et al. (2001) which adopts the optical constants of Draine & Lee (1984) for silicates, Warren (1984) for water ice, and Greenberg & Li (1996) for organics. We consider the total opacity due to both true absorption and scattering, $\chi_\nu = \kappa_\nu + \sigma_\nu$, where κ_ν and σ_ν are the absorption and scattering mass coefficients,

respectively. For a given maximum grain size a_{max} and dust-to-gas mass ratio $\zeta = \epsilon \zeta_{ISM}$, one computes the mean and monochromatic opacities to calculate the vertical structure and the emission of the models.

In these models, the disk is heated by viscous dissipation, stellar and accretion irradiation, and a warm envelope (D'Alessio et al. 1997), and cools by dust emission. We assume the dust and the gas are thermally coupled by collisions and have the same temperature. To obtain the vertical structure and emission of the disk, we follow the formalism of Lizano et al. (2016) without magnetic field, where the disk temperature T and gas density ρ at each radius are calculated as a function of the mass surface density variable (see their Equations (11)–(13) and (17)–(18)), and the total disk flux has a viscous and a reprocessed component. The latter is due to the disk surface irradiation. For the irradiation of the envelope we assume a thermal bath at the disk surface, with a temperature profile $T_e = T_0(R/100\ au)^{-q}$ (see Tapia & Lizano 2017). This warm envelope prevents the outer radii of the disks from becoming too cold and has been used to reproduce the millimeter SED and profiles of HL Tau (e.g., D'Alessio et al. 1997; Tapia & Lizano 2017). For all models we use $T_0 = 35$ K and $q = 0.16$ which is enough to heat the disk outer regions.

5. The Observed Millimeter Profiles of HL Tau

We compare the emission of the models with HL Tau millimeter images at 870 μm and 1.3 mm (ALMA Partnership et al. 2015), and 2.1 mm (ALMA), and 7.8 mm (VLA) from CG19. The VLA image at $\lambda = 7.8$ mm is a combination between the Ka and Q bands, which are decontaminated from free–free emission. The images at all wavelengths are convolved to an angular resolution of 50 mas (7.35 AU at 147 pc). The intensity profiles shown in Figures 2–9 below correspond to the azimuthally averaged intensity profiles of the disk maps taking into account the disk inclination. We find that with an inclination angle $i^{model} = 37°$, the convolved model images shown below have an aspect ratio between the major and minor axes that corresponds to the inclination inferred from the observed maps $i^{obs} \sim 47°$. Finally, because the signal-to-noise of the VLA 7.8 mm image is poor beyond 60 au, we will only compare the model's emission within this radius.

6. The Multiwavelength Emission Level

In this section, we aim to obtain the dust properties in the disk that can reproduce the level of emission along the observed profiles simultaneously at all 4 mm wavelengths. We will discuss the profile's substructure in the next section.

To compare the emission of the models with the observed azimuthally averaged ALMA and VLA profiles of HL Tau at 0.87, 1.2, 2.1, and 7.8 mm, we vary the maximum grain size a_{max} and the dust-to-gas mass ratio of the disk models. We explore models with $a_{max} = 100\ \mu$m, 1 mm, and 1 cm. We also consider these different values of a_{max} in the disk atmosphere and the disk midplane. In this section, we assume a dust-to-gas mass ratio $\zeta = \epsilon\ \zeta_{ISM}$ with a constant dust ratio $1 \leqslant \epsilon \leqslant 9$. As discussed above, such values for the dust ratio are found, for example, in protoplanetary disks in the Lupus star-forming region (Ansdell et al. 2016). Table 2 shows the different models that we discuss below. Figure 1 shows a sketch of the different models.
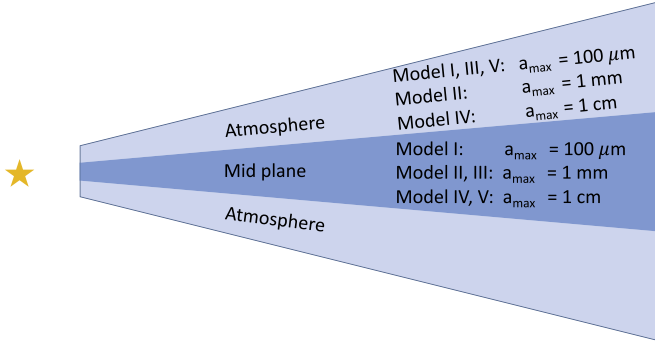
Figure 1. Sketch of the atmosphere and midplane of the different models in Table 2.
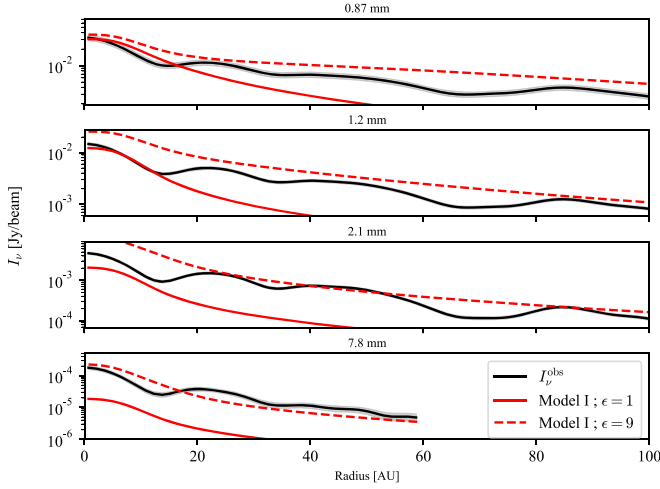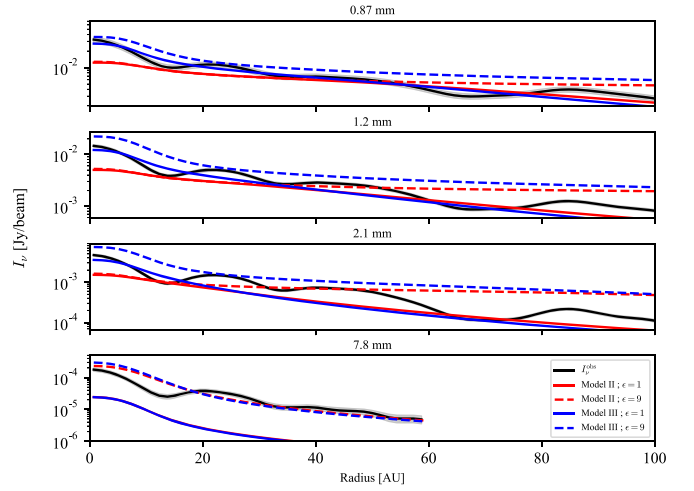

Figure 2. Black solid lines show the observed azimuthally averaged profiles at each wavelength. The black solid lines surrounding these profiles correspond to the error bars. The gray lines show the profiles of Model I with a dust-to-gas mass ratio $\zeta = \epsilon \zeta_{ISM}$, with a dust ratio $\epsilon = 1$ (solid lines) and $\epsilon = 9$ (dashed lines).

Table 2
Models of Dust Size Distribution

Model	Atmosphere a_{max}	Midplane a_{max}
I	100 μm	100 μm
II	1 mm	1 mm
III	100 μm	1 mm
IV	1 cm	1 cm
V	100 μm	1 cm

Figure 2 shows (black solid lines) the observed azimuthally averaged profiles at each wavelength indicated on the top of each panel: 0.87, 1.2, 2.1, and 7.8 mm, from top to bottom. The gray solid lines surrounding these profiles correspond to the error bars that take into account the rms and systematic errors due to the flux calibration (see the detailed discussion in CG19). The red lines show the profiles of Model I: a disk with $a_{max} = 100\ \mu$m in both the atmosphere and the midplane. The solid red lines correspond to a dust-to-gas mass ratio $\zeta = \epsilon \zeta_{ISM}$ with a dust ratio $\epsilon = 1$; the red dashed lines correspond to a dust ratio $\epsilon = 9$. This high value of the dust ratio can reproduce the level of emission at all four wavelengths in the external part of the disk ($R > 40$ au) although the emission is a bit low at 7.8 mm. Moreover, the

Figure 3. Black solid lines show the observed profiles at each wavelength. The red lines show the profiles of Model II with a dust-to-gas mass ratio $\zeta = \epsilon \zeta_{ISM}$, with a dust ratio $\epsilon = 1$ (solid lines) and $\epsilon = 9$ (dashed lines). The blue lines show the profiles of Model III with a dust ratio $\epsilon = 1$ (solid lines) and $\epsilon = 9$ (dashed lines).
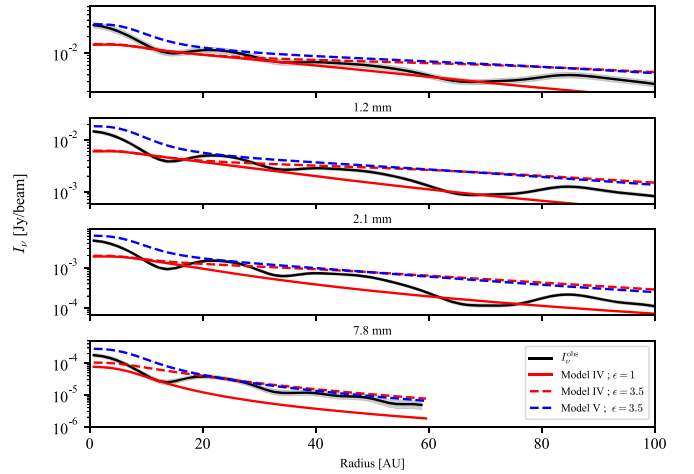
Figure 4. Black solid lines show the observed profiles at each wavelength. The red lines show the profiles of Model IV with a dust-to-gas mass ratio $\zeta = \epsilon \zeta_{ISM}$ with a dust ratio $\epsilon = 1$ (solid lines), and a dust ratio $\epsilon = 3.5$ (dashed lines). The dashed blue lines show the profiles of Model V with a dust ratio $\epsilon = 3.5$.

Table 3
Model VI ($\epsilon = 3.5$)

Atmosphere	$a_{max} = 100\ \mu$m
Gaps midplane	$a_{max} = 100\ \mu$m
Rings midplane	$a_{max} = 1$ cm

model profiles at 1.2 and 2.1 mm have too much emission at the inner region.

Figure 3 shows as black solid lines the observed profiles at each wavelength. Each panel shows 2 models, each with 2 values of the dust ratio ϵ. The red lines show the profiles of Model II: a disk with $a_{max} = 1$ mm in both the atmosphere and the midplane. The solid red lines correspond to a dust-to-gas mass ratio $\zeta = \epsilon \zeta_{ISM}$ with a dust ratio $\epsilon = 1$; the dashed red lines correspond to a dust ratio $\epsilon = 9$. The blue lines show the profiles of Model III: a disk with $a_{max} = 100\ \mu$m in the

Table 4
Model VII ($\epsilon(R)$)

Atmosphere: $a_{max} = 100\,\mu$m| Midplane: $a_{max} = 1$ cm							
$R/$au[a]	<7.5	[7.5–16.5]	16.5–32	[32–40]	40–60	[60–90]	90–100	[>100]
$\epsilon\,(R)$	1.5	0.1	3.5	0.8	3.5	1.0	3.5	1.5

Note. (a) Gaps are indicated with brackets.

atmosphere and 1 mm in the midplane. The solid blue lines correspond to a dust-to-gas mass ratio $\zeta = \epsilon\zeta_{ISM}$ with a dust ratio $\epsilon = 1$; the dashed blue lines correspond to a dust ratio $\epsilon = 9$. This large value of ϵ can reproduce the level of emission at 7.8 mm but the models have too much emission for radii $R > 50$ au, especially the 2.1 mm profile.

Figure 4 shows (black solid lines) the observed profiles at each wavelength. This figure also shows 2 models with different values of the dust ratio ϵ. The red lines show the profiles of Model IV: a disk with $a_{max} = 1$ cm in both the atmosphere and the midplane. The solid red lines correspond to a dust-to-gas mass ratio $\zeta = \epsilon\zeta_{ISM}$ with a dust ratio $\epsilon = 1$; the dashed red lines correspond to a a dust ratio $\epsilon = 3.5$. The dashed blue lines show the profiles of Model V, a disk with $a_{max} = 100\,\mu$m in the atmosphere and 1 cm in the midplane, with a dust ratio $\epsilon = 3.5$.[4] The latter model can reproduce the level of emission of the observed multiwavelength profiles with a moderate dust-to-gas mass ratio, a factor of 3.5 the ISM value. Thus, we will use this model to study the profile's substructure in the next section.

7. Disk Substructure: Rings and Gaps

The disk of HL Tau has a dark–bright ring substructure. In this section we explore if the fainter emission in the gaps can be produced by changing the grain size or the amount of dust mass in the gaps with respect to the rings, in order to decrease the optical depth.[5] In the first case, one considers a dust distribution in the gaps with a_{max} smaller than in the rings. In the second case, one considers the same dust, but a smaller dust ratio ϵ in the gaps than in the rings. To explore the effect of changing the dust properties in the gaps, they are located in the range of radii $6.5 < R/\text{au} < 16.5$, $31 < R/\text{au} < 40$, $60 < R/\text{au} < 86$, and $R/\text{au} > 100$, consistent with the gap locations given by ALMA Partnership et al. (2015).

Differences in the dust grains sizes and/or dust mass between gaps and rings are expected, for example, when planets produce gaps where the dust is depleted and also induce pressure bumps at the gap edges. These pressure maxima act as dust traps where dust particles with large Stokes parameters accumulate, while the smaller dust particles remain in the gaps, coupled with the gas (e.g., Zhang et al. 2018). Dust trapping is also produced in ring pressure maxima (e.g., Sierra et al. 2019); or outside the snow lines of different volatiles where sintering suppresses dust growth and produces a pile up of small dust grains (e.g., Okuzumi et al. 2016). Figure 7 of CG19 shows that the grain sizes and dust surface density in the gaps of HL Tau are smaller than in the rings. In their work the dust properties are inferred by modeling the radial dust spectral indices, assuming an isothermal vertical structure. Their inferred

contrasts in dust properties between gaps and rings are limited by the spatial resolution of the observations (see the discussion in their Section 4.2).

Table 3 shows the parameters of Model VI, which decreases the opacity in the gaps by decreasing the size of the dust particles. This model has grains with $a_{max} = 100\,\mu$m in the atmosphere; in the midplane it has grains with $a_{max} = 1$ cm in the rings, and grains with $a_{max} = 100\,\mu$m in the gaps. Table 4 shows the parameters of Model VII, which has a deficit of dust mass in the gaps. This model has $a_{max} = 100\,\mu$m in the atmosphere and $a_{max} = 1$ cm in the midplane. The dust ratio is a function of radius, $\epsilon\,(R)$. Figure 5 shows the dust surface density profile of this model.

Figure 6 shows the observed millimeter profiles together with the profiles of Models VI and VII. The green lines correspond to Model VI. The red lines correspond to Model VII. Model VI, which explores the opacity effect of small grains in the gaps, has excess emission at the ALMA wavelengths in the first gap and beyond ∼60 au. Model VII, which explores a mass deficit in the gaps, reproduces reasonably well the gaps and rings for the assumed function $\epsilon\,(R)$. A combination of both a mass deficit and an opacity effect would also reproduce the observed substructure.

8. Changing the Disk Parameters

To explore the effect of changing the dust settling, we consider model VII with different settling parameters $s_{big} = 0.2$, 0.4, and 0.6 and different dust ratios $\epsilon_{small} = 0.1$ and 0.01. The settling parameters $s_{big} = 0.2$, 0.4, and 0.6 correspond to a dust scale height δH, with $\delta = 0.25$, 0.53, and 0.84, respectively (Appendix), where the gas scale height H is evaluated at the midplane temperature.

Figure 7 shows the effect of varying s_{big} in the model profiles, keeping the same $\epsilon_{small} = 0.1$. The red, green, and blue lines correspond to the model with $s_{big} = 0.6$, 0.4, and 0.2, respectively, where $s_{big} = 0.4$ corresponds to Model VII. Figure 8 shows the ratios of the model and the observed intensity at each wavelength. The code color is the same as that in Figure 7. The solid and dashed lines correspond to models with $\epsilon_{small} = 0.1$ and 0.01, respectively. The χ^2 value of each model is calculated as

$$\chi^2 = \sum_{\nu} \chi_{\nu}^2 = \sum_{\nu} \left[\frac{1}{N_\nu} \sum_{j=1}^{N_\nu} \frac{(I_\nu^{\text{model}} - I_\nu^{\text{obs}})^2}{(I_\nu^{\text{obs}})^2} \right], \qquad (11)$$

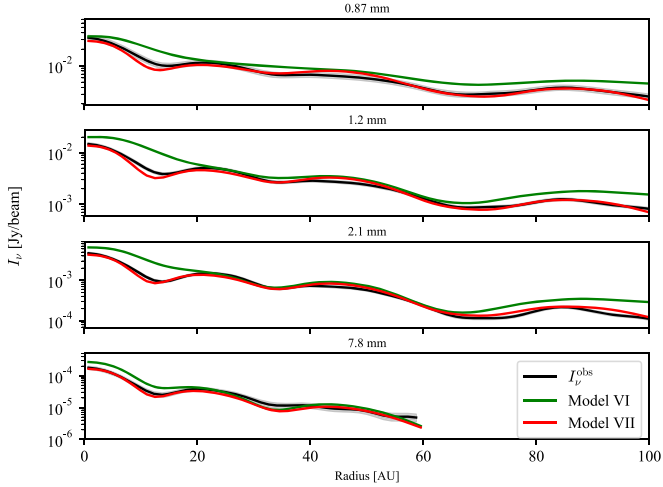where one sums over N_ν radii. These values are shown in Table 5.

Figure 9 shows the effect of changing the initial mass accretion rate $\dot{M}_{*0}$ and disk mass M_{d0} in Model VII. From Equations (7) and (9) one can see that the mass surface density increases with M_{d0}, and decreases with $\dot{M}_{*0}$. The viscosity has the opposite dependence on these parameters (see Equation (10)) and affects the temperature mainly in the active regions located at the disk midplane, while the stellar irradiation determines the temperature

---
[4] We omit Model V with $\epsilon = 1$ because it does not have enough emission at 7.8 mm.

[5] We note that the temperature is not a free parameter of the model, but is obtained from local processes of dust heating and cooling.
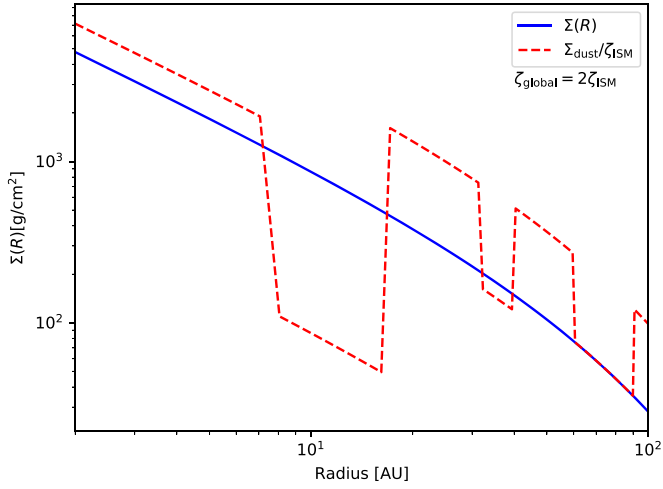
Figure 5. Solid blue line shows the gas surface density radial profile $\Sigma(R)$ of the viscous disk. The dashed red line shows the normalized dust surface density radial profile of Model VII: $\Sigma_{dust}/\zeta_{ISM}$. The global dust-to-gas mass ratio of the disk in this model is $\zeta_{global} = 2\zeta_{ISM}$.

Figure 7. Black solid lines show the observed profiles at each wavelength. The red, green, and blue solid lines show the profiles of Model VI where $s_{big} = 0.6$, 0.4, and 0.2, respectively. The red lines correspond to Model VII.

Figure 6. Black lines show the observed profiles at each wavelength. The green lines show the profiles of Model VI. The red lines show the profiles of Model VII.
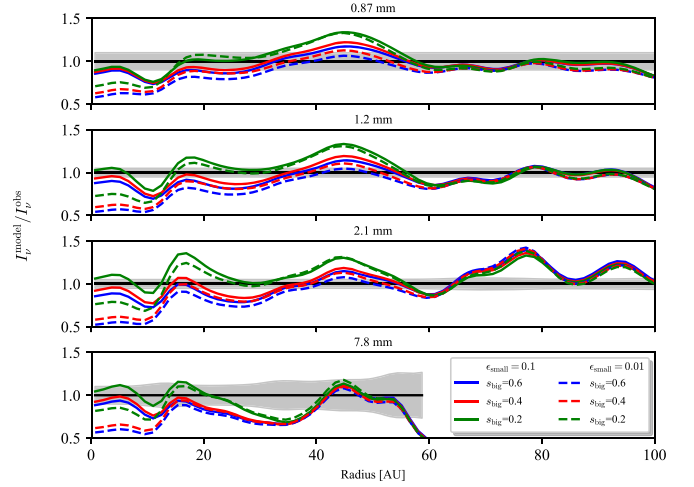
Figure 8. Panels show the ratios of the model and observed intensities at each wavelength. The gray shadows correspond to the error bars. The red, green, and blue lines correspond to $s_{big} = 0.6$, 0.4, and 0.2, respectively. The solid and dashed lines correspond to models with $\epsilon_{small} = 0.1$ and 0.01, respectively. The solid red lines ($s_{big} = 0.4$; $\epsilon_{small} = 0.1$) correspond to Model VII.
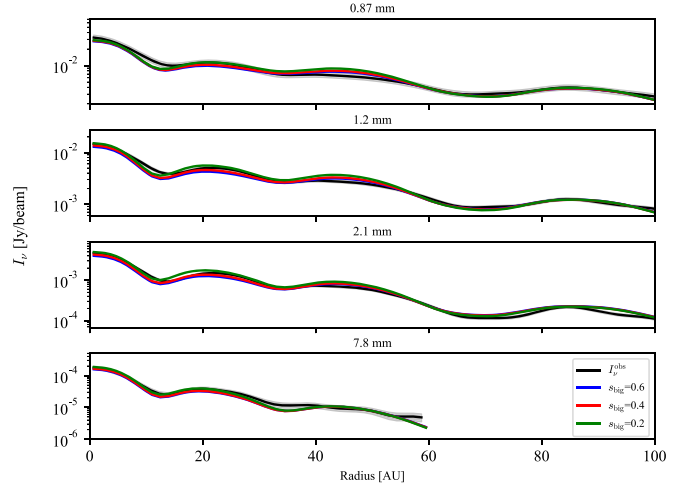
of the upper layers (see, e.g., Figure 4 of Lizano et al. 2016). In these models the disk emission is mainly affected by changes in the mass surface density, such that the optically thin emission increases with the initial disk mass M_{d0}, and, for a given M_{d0}, the emission decreases with the initial mass accretion rate $\dot{M}_{*0}$.

Finally, Figure 10 shows the effect of changing the power-law viscosity exponent to $\gamma = 0$, keeping the same parameters of model VII. In this case the viscosity is independent of radius,

$$\nu = \nu_1 = \frac{4}{3}\frac{\dot{M}_{*0}R_c^2}{M_d(0)}\mathbb{T}^{-1}. \qquad (12)$$

The surface density depends on the radius only through the exponential function,

$$\Sigma(r, \mathbb{T}) = \frac{M_d(0)}{\pi R_c^2}\mathbb{T}^{-1/4}\exp(-r^2), \qquad (13)$$

Table 5
χ^2 for Different Models

| ϵ_{small} s_{big}	0.2	0.4	0.6
0.1	0.14	0.12	0.13
0.01	0.16	0.19	0.23

and the mass accretion rate is

$$\dot{M}(r, \mathbb{T}) = \dot{M}_{*0}\mathbb{T}^{-5/4}\exp(-r^2)[1 - 4r^2], \qquad (14)$$

where $r = R/R_c$ and $R_c = R_l\mathbb{T}^{1/2}$. In addition, the nondimensional time is

$$\mathbb{T} = 8t_{age}\frac{\dot{M}_{*0}}{M_{d0}} + 1. \qquad (15)$$
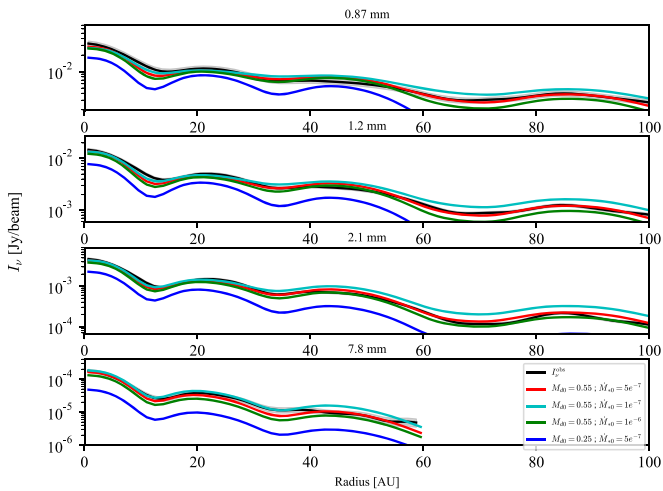
Figure 9. Black solid lines show the observed profiles at each wavelength. The different colored lines show models where the initial disk mass M_{d0} and the initial mass accretion rate $\dot{M}_{*0}$ vary with respect to Model VII, which corresponds to the red solid lines.
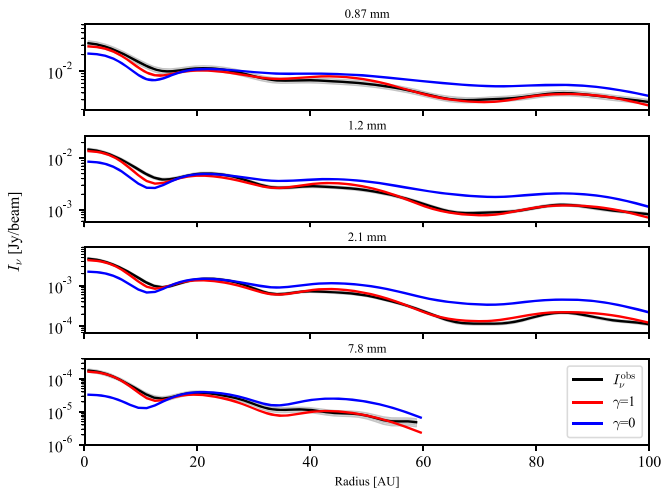
Figure 10. Black solid lines show the observed profiles at each wavelength. The red solid lines show the profiles of Model VII. The blue lines show the profiles of a model with a viscosity power-law exponent $\gamma = 0$.

One can see that the model with $\gamma = 0$ is flatter than the observed profiles.

9. Discussion

In the previous section we calculate the emission of the Lynden-Bell & Pringle evolutionary disks with a viscosity power-law exponent $\gamma = 1$, with different dust properties, in order to reproduce the level of emission of the observed ALMA and VLA profiles. For each model, we adjust the dust ratio ϵ to obtain the amount of dust mass needed to achieve the observed level of the 7.8 mm VLA emission at the outer disk radii ($40 < R/\mathrm{au} < 60$).

We found that Model I, composed of small grains with a size distribution with $a_{\max} = 100\,\mu$m in both the atmosphere and the midplane, requires a large value of the dust ratio $\epsilon \sim 9$ to fit the outer radii of the 7.8 mm profile (Figure 2). Nevertheless, with this amount of dust, the model profiles at the ALMA wavelengths show excess emission at the inner region of the

disk ($R < 20$ au). Thus, this is not a good model to produce the observed dust emission at all four wavelengths.

Models II and III, which have larger grains with $a_{\max} = 1$ mm in the midplane and $a_{\max} = 100\,\mu$m or $a_{\max} = 1$ mm in the atmosphere (see Table 2), also require a large dust ratio $\epsilon = 9$ to fit the 7.8 mm VLA profile. One can see in Figure 3 that the level of emission in the inner disk of the 3 ALMA profiles is obtained only with Model III, where the atmosphere has a grain size distribution with $a_{\max} = 100\,\mu$m, since these particles absorb the stellar radiation more efficiently producing a hotter inner region, compared to Model II. Also, for the same value of ϵ, both Models II and III produce very similar levels of 7.8 mm emission because the small grains in the atmosphere of Model III do not contribute at this wavelength. Nevertheless, for $R > 50$ au, both models with the $\epsilon = 9$, have excess emission at ALMA wavelengths: the same dust needed to reproduce the level of the 7.8 mm emission, produces too much emission at these wavelengths.

Model IV, which has $a_{\max} = 1$ cm in both the atmosphere and the midplane, requires much less dust than the previous models, $\epsilon = 3.5$, to reproduce the level of the 7.8 mm emission for $R > 20$ au. Nevertheless, this model has a deficit of emission in the inner disk region $R < 15$ au at all wavelengths (Figure 4).

Model V, which has an atmosphere with $a_{\max} = 100\,\mu$m, and the midplane with $a_{\max} = 1$ cm, is able to produce the level of emission of all the observed profiles with $\epsilon = 3.5$, a dust-to-gas mass ratio a factor of 3.5 the ISM value. The smaller grains in the atmosphere absorb the stellar radiation more efficiently than the larger grains of Model IV, heating the inner disk region and increasing the emission at all wavelengths. In addition, the large centimeter grains in the disk contribute to the 7.8 mm emission in the outer disk region, without producing excess emission at the ALMA wavelengths. Thus, the dust size distribution of Model V is favored over the other models.

To fit the profile's substructure (bright rings and dark gaps) at ALMA and VLA wavelengths, we consider variations of Model V where the optical depth is changed in the gaps (Models VI and VII; see Figure 6). Model VI, which has a grain size distribution with $a_{\max} = 100\,\mu$m in the atmosphere and in the gaps, and $a_{\max} = 1$ cm in the midplane of the rings, has a smaller opacity in the gaps because the $100\,\mu$m particles have a smaller monochromatic opacity than the 1 cm particles in the rings (see, e.g., Figure 10 of Sierra et al. 2017). This model has an excess of emission in the first gap at ALMA wavelengths because the gas is hot. It also has excess emission beyond 60 au. Model VII, which has a grain size distribution with $a_{\max} = 100\,\mu$m in the atmosphere and $a_{\max} = 1$ cm in the midplane, as well as a deficit of dust mass in the gaps with respect to the rings ($\epsilon(R)$; see Table 4), can reproduce the ring–gap substructure. In fact, a hybrid model with a smaller opacity in the gaps ($a_{\max} = 100\,\mu$m) like Model VI and a dust mass deficit in the rings could also reproduce the ring–gap substructure. As discussed above, it is possible that both effects are at work, given that planet formation, dust trapping in pressure maxima, and sintering due the different volatile snow lines will decrease the dust mass and change the grain size in the gaps (e.g., Zhang et al. 2018, Okuzumi & Tazaki 2019, Sierra et al. 2019).

Because of the mass deficit in the gaps, Model VII has a global dust-to-gas mass ratio $\zeta_{\mathrm{global}} = 2\,\zeta_{\mathrm{ISM}}$ within a 100 au.
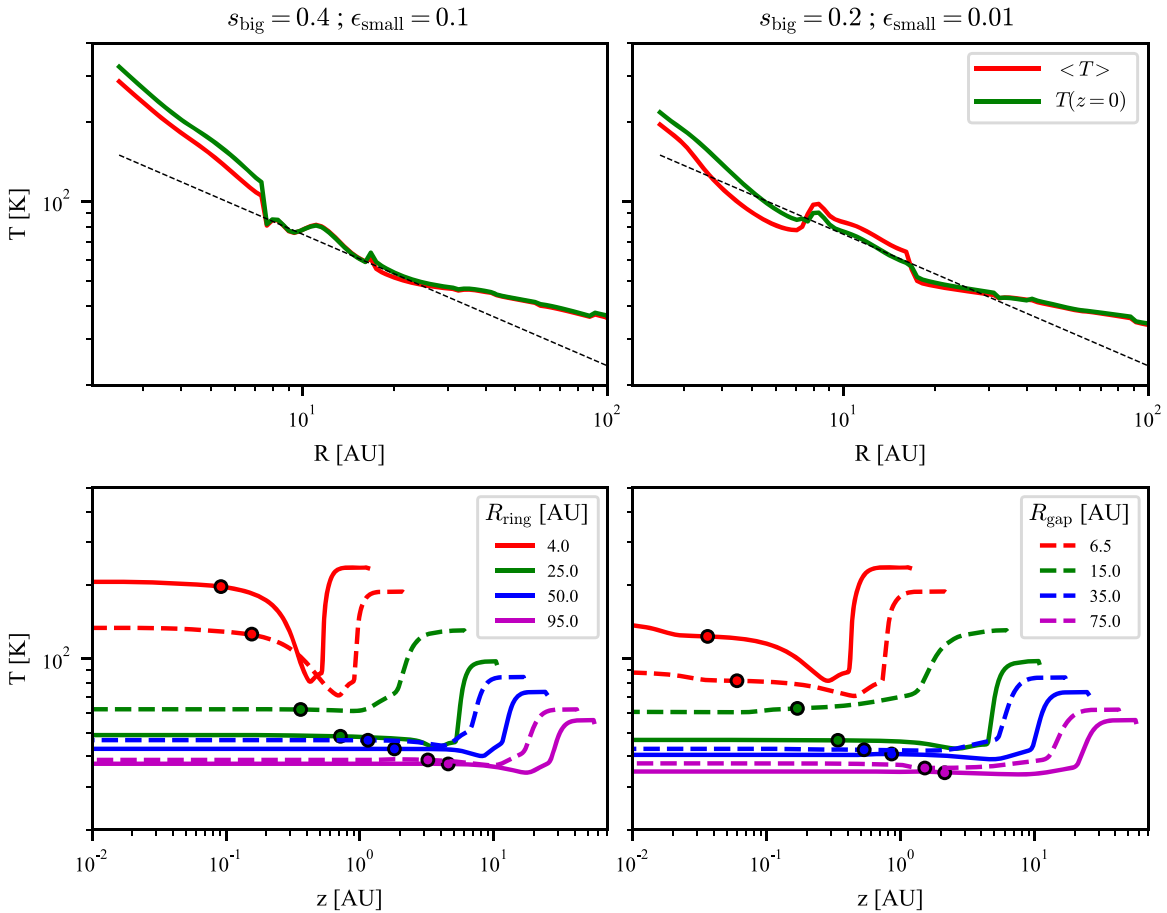
Figure 11. Disk structure for $s_{\rm big} = 0.4$ and $\epsilon_{\rm small}$=0.1 (left panels); and $s_{\rm big} = 0.2$ and $\epsilon_{\rm small} = 0.01$ (right panels). The top panels show the average temperature (red lines) ($\langle T \rangle = \int T \rho dz / \Sigma_\varpi$) and the midplane temperature (green lines) as a function of radius. The black dashed lines have a slope $p = -0.5$. The bottom panels show the temperature as a function of height above the midplane for different radii. The solid lines correspond to radii inside the rings. The dashed lines correspond to radii inside the gaps. The open dots show the location of settling height $z_{\rm big}$ at each radius.

Since the gas mass of the disk is $M_d(100 \text{ au}, 1 \text{ Myr}) = 0.23 M_\odot$ (Equation (3)), the dust mass within this radius is $M^{\rm dust} = \zeta_{\rm global} M_d = 4.8 \times 10^{-3} M_\odot$. This is the amount of dust required to produce the observed 7.8 mm emission. These values are a factor of 10 times higher than those obtained by Carrasco-González et al. (2016) and CG19, who used a vertically isothermal structure to infer the disk temperature, in contrast with the vertical structure models considered in this work.

We explored the effect of changing the dust settling parameters $s_{\rm big}$ and $\epsilon_{\rm small}$ in Model VII. The differences occur mainly inside $R \gtrsim 50$ au. One finds that with a degree of settling $\epsilon_{\rm small} = 0.1$, the model with the smallest χ^2 has $s_{\rm big} = 0.4$ (a dust scale height $0.53H$). For a more extreme degree of settling $\epsilon_{\rm small} = 0.01$, the model with the smallest χ^2 has $s_{\rm big} = 0.2$ (a dust scale height $0.25H$). Figure 11 shows radial and vertical temperature structure of these two models. The radial profiles show that in the inner region, the disk with smaller settling height ($s_{\rm big} = 0.2$) is colder than the model with $s_{\rm big} = 0.4$. These temperature profiles are comparable to the temperature profile found by Liu et al. (2017) for the HL Tau disk. The sharp temperature transitions between rings and gaps are due to the fact that, for simplicity, we assumed a sharp change in the dust properties and calculated a 1D vertical structure, which neglects radial gradients. For reference, the

dashed black lines show a slope $p = -0.5$. The vertical profiles show that, for both models, except for the first ring, the gaps (dashed lines) are warmer than the rings (solid lines). The open circles show the location of the settling height $z_{\rm big}$ at each radius, the boundary of the midplane region which has large grains.

We considered evolutionary disks with a smaller initial disk mass and different initial mass accretion rates than Model VII (Figure 9). The emission of these models vary mainly due to the change in the mass surface density (see Equations (9) and 7). For example, consider the model with a disk initial mass $M'_{d0} = 0.25 M_\odot$, and an initial mass accretion rate $\dot{M}_{*0} = 5 \times 10^{-7} M_\odot \text{yr}^{-1}$, which has a disk mass $M'_d(100 \text{ au}, 1 \text{ Myr}) = 8.0 \times 10^{-2} M_\odot$, three times smaller than that of Model VII. Given the amount of dust required by Model VII ($M^{\rm dust} = 4.8 \times 10^{-3} M_\odot$) to produce the 7.8 mm emission, one can estimate that this model would need a global dust-to-gas mass ratio $\zeta' = M^{\rm dust}/M'_d = 6 \zeta_{\rm ISM}$ to reach the same level of emission.

Finally, we explore an evolutionary disk with the same parameters as Model VII, but with a viscosity power-law exponent $\gamma = 0$, closer to the exponent $\gamma = 0.2$, used for the functional form of the disk surface density by several authors (e.g., Kwon et al. 2015; Pinte et al. 2016; Liu et al. 2017). Since the initial disk mass is the same in both models, the surface

density of the $\gamma = 0$ model is lower at the center and higher at the outer regions, with respect to the $\gamma = 1$ model. For this reason, the emission profiles are flatter than the $\gamma = 1$ model: there is a deficit of emission at the center and an excess of emission at the outer disk regions.

10. Conclusions

We probe the dust grain properties in the disk of HL Tau using the disk evolutionary models of Lynden-Bell & Pringle with a viscosity power-law exponent $\gamma = 1$ by comparing the models' emission with multiwavelength ALMA and VLA profiles. This comparison favors disks with a dust size distribution with small grains in the atmosphere ($a_{max} = 100\,\mu m$) and large grains in the midplane ($a_{max} = 1\,cm$).

The bright and dark ring substructure in the observed profiles can be reproduced by changing the optical depth in the gaps. This can be done by either a change in opacity (small grains in the gaps with $a_{max} = 100\,\mu m$) or a dust mass deficit in the gaps (a dust ratio $\epsilon(R)$ larger in the rings than in the gaps), or a combination of both. The model that reproduces the multi-wavelength ALMA and VLA profiles of HL Tau has a global dust-to-gas mass ratio two times the ISM value and contains a total dust mass $M^{dust} = 4.8 \times 10^{-3}\,M_\odot$ within 100 au. This dust mass is required to achieve the emission level of the 7.8 mm VLA profile.

In the evolutionary models, decreasing the initial disk mass or increasing the initial mass accretion rate with respect to the fiducial model, decreases the mass surface density and thus, decreases the emission at 7.8 mm. A dust scale height between 0.3 and 0.5 of the gas scale height H can fit the observed profiles. In addition, the millimeter emission profiles of a model with a mass surface density with a power-law exponent $\gamma = 0$, are flatter than the observed ALMA and VLA profiles.

Although we focused on a specific evolutionary model where the disk structure and emission can be calculated self-consistently, we conclude from this work that the high resolution optically thin millimeter (VLA) observations are very important to determine the dust properties and dust mass in protoplanetary disks. With such data, it will be possible to infer the dust properties of many more protoplanetary disks in the near future.

Appendix
Dust Settling

In this appendix we rewrite the formalism of D'Alessio et al. (2006) in terms of the gas surface density, including a dust-to-gas mass ratio that can be a function of radius $\zeta(R)$.[6] These authors assume that the dust settles to the midplane and grows. Then, the disk has a distribution of small grains in the upper layers (e.g., $a_{max} = 1$–$100\,\mu m$) and a distribution of big grains (e.g., $a_{max} = 1\,mm$–$1\,cm$) in the midplane. At each radius, the total gas mass surface density is $\Sigma(R) = 2\int_0^\infty \rho\,dz$ where ρ is the volume density and z is the height over the disk midplane.

The total surface density can be written in terms of the surface density of the midplane layers with big grains $\Sigma_{big} = 2\int_0^{z_{big}} \rho\,dz$,

---

[6] $\zeta(R)$ can be the ISM value $\zeta_{ISM} = 1/100$ or another value that takes into account, e.g., dust radial migration and/or dust depletion in gaps.

where z_{big} is the height of the midplane region, and the surface layers with small grains $\Sigma_{small} = 2\int_{z_{big}}^\infty \rho\,dz$,

$$\Sigma(R) = \Sigma_{big} + \Sigma_{small}. \qquad (16)$$

Originally, the surface and midplane layers had the same dust-to-gas mass ratio $\zeta(R)$. Due to settling, the surface layers lost dust such that they now have a smaller dust-to-gas mass ratio ζ_{small}. Then, the dust mass lost by the upper layers is given by the original dust mass minus the dust mass that remains in these layers

$$\Sigma_{up,lost}^d = (\zeta(R) - \zeta_{small})\Sigma_{small}. \qquad (17)$$

The midplane layers have a dust surface density given by the original dust mass plus the mass of settled grains from the upper layers,

$$\Sigma_{down}^d = [\zeta(R)\Sigma_{big} + (\zeta(R) - \zeta_{small})\Sigma_{small}] \equiv \zeta_{big}\Sigma_{big}. \qquad (18)$$

This equation defines the midplane dust-to-gas mass ratio ζ_{big}. This equation can be rewritten in terms of the dust ratios $\epsilon(R) = \zeta(R)/\zeta_{ISM}$, $\epsilon_{small} = \zeta_{small}/\zeta_{ISM}$, and $\epsilon_{big} = \zeta_{big}/\zeta_{ISM}$ as

$$\epsilon_{big} = \epsilon(R) + (\epsilon(R) - \epsilon_{small})\frac{\Sigma_{small}}{\Sigma_{big}}$$
$$= \epsilon(R) + (\epsilon(R) - \epsilon_{small})\left(\frac{\Sigma(R)}{\Sigma_{big}} - 1\right), \qquad (19)$$

where the last equality comes from Equation (16). In the case $\zeta(R) = \zeta_{ISM}$, $\epsilon(R) = 1$, and

$$\epsilon_{big} = 1 + (1 - \epsilon_{small})\left(\frac{\Sigma(R)}{\Sigma_{big}} - 1\right). \qquad (20)$$

For example, for $\epsilon_{small} = 0.1$, and $\Sigma_{big}/\Sigma(R) = 0.6$, this equation gives $\epsilon_{big} = 1.6$.

To avoid problems of convergence in the code of the vertical structure, one makes a smooth transition between the upper and lower layers and calculates the dust ratio ϵ as a function of the surface density measured from the midplane $\sigma = 2\int_0^z \rho\,dz$ as

$$\epsilon_{small}(\sigma) = \frac{\zeta_{small}(\sigma)}{\zeta_{ISM}} = 0.5\epsilon_{small}\left(1 - \tanh\left[k\left(1 - \frac{\sigma}{\sigma_{big}}\right)\right]\right), \qquad (21)$$

and

$$\epsilon_{big}(\sigma) = \frac{\zeta_{big}(\sigma)}{\zeta_{ISM}} = 0.5\,\epsilon_{big}\left(1 + \tanh\left[k\left(1 - \frac{\sigma}{\Sigma_{big}}\right)\right]\right), \qquad (22)$$

where $0 < \sigma < \Sigma(R)$.

In addition, the relation between the settling height z_{big} and the midplane mass surface density Σ_{big} can be easily obtained for a vertically isothermal disk where the density is given by

$$\rho = \rho_0\exp\left(\frac{-z^2}{2H^2}\right), \qquad (23)$$

Tapia et al.

where z is the vertical coordinate and H is the disk scale height. In this case, the total gas mass surface density is given by

$$\Sigma(R) = 2 \int_0^\infty \rho_0 \exp\left(\frac{-z^2}{2H^2}\right) dz = \sqrt{2\pi} H \rho_0. \quad (24)$$

If one writes $z_{\text{big}} = \delta H$,

$$\Sigma_{\text{big}} = 2 \int_0^{\delta H} \rho_0 \exp\left(\frac{-z^2}{2H^2}\right) dz = \sqrt{2\pi} H \rho_0 \, \text{erf}\left(\frac{\delta}{\sqrt{2}}\right). \quad (25)$$

Then, the factor δ is given by the trascendental equation

$$\frac{\Sigma_{\text{big}}}{\Sigma(R)} = \text{erf}\left(\frac{\delta}{\sqrt{2}}\right). \quad (26)$$

For example, for $\Sigma_{\text{big}}/\Sigma(R) = 0.6$ and 0.2, $z_{\text{big}} = 0.84H$ and $0.25H$, respectively.

For nonisothermal disks, the height coefficient δ can be found directly from the disk vertical structure, evaluating the scale height at the midplane temperature.

ORCID iDs

Carlos Tapia ⓘ https://orcid.org/0000-0002-2196-1447
Susana Lizano ⓘ https://orcid.org/0000-0002-2260-7677
Anibal Sierra ⓘ https://orcid.org/0000-0002-5991-8073
Carlos Carrasco-González ⓘ https://orcid.org/0000-0003-2862-5363

References

ALMA Partnership, Brogan, C. L., Pérez, L. M., et al. 2015, ApJL, 808, L3
Andrews, S. M., Huang, J., Pérez, L. M., et al. 2018, ApJL, 869, L41
Ansdell, M., Williams, J. P., van der Marel, N., et al. 2016, ApJ, 828, 46
Brauer, F., Dullemond, C. P., & Henning, T. 2008, A&A, 480, 859
Carrasco-González, C., Henning, T., Chandler, C. J., et al. 2016, ApJL, 821, L16
Carrasco-González, C., Sierra, A., Flock, M., et al. 2019, ApJ, 883, 71, (CG19)
D'Alessio, P., Calvet, N., & Hartmann, L. 1997, ApJ, 474, 397
D'Alessio, P., Calvet, N., & Hartmann, L. 2001, ApJ, 553, 321
D'Alessio, P., Calvet, N., Hartmann, L., et al. 2006, ApJ, 638, 314
Dipierro, G., Price, D., Laibe, G., et al. 2015, MNRAS, 453, L73
Dong, R., Li, S., Chiang, E., et al. 2018, ApJ, 866, 110
Draine, B. T., & Lee, H. M. 1984, ApJ, 285, 89
Flock, M., Ruge, J. P., Dzyurkevich, N., et al. 2015, A&A, 574, A68
Galli, P. A. B., Loinard, L., Ortiz-Léon, G. N., et al. 2018, ApJ, 859, 33
Greenberg, J. M., & Li, A. 1996, A&A, 309, 258
Gullbring, E., Hartmann, L., Briceño, C., et al. 1998, ApJ, 492, 323
Hartmann, L., Calvet, N., Gullbring, E., et al. 1998, ApJ, 495, 385
Jin, S., Li, S., Isella, A., et al. 2016, ApJ, 818, 76
Kataoka, A., Muto, T., Momose, M., et al. 2015, ApJ, 809, 78
Kataoka, A., Tsukagohi, T., Pohl, A, et al. 2017, ApJL, 844, L5
Kwon, W., Looney, L. W., & Mundy, L. G. 2011, ApJ, 741, 3
Kwon, W., Looney, L. W., Mundy, L. G., et al. 2015, ApJ, 808, 102
Liu, Y., Henning, T., Carrasco-González, C., et al. 2017, A&A, 607, A74
Lizano, S., Tapia, C., Boehler, Y., et al. 2016, ApJ, 817, 35
Lynden-Bell, D., & Pringle, J. E. 1974, MNRAS, 168, 603
Mathis, J. S., Rumpl, W., & Nordsieck, K. H. 1977, ApJ, 217, 425
Okuzumi, S., Momose, M., Sirono, S., et al. 2016, ApJ, 821, 82
Okuzumi, S., & Tazaki, R. 2019, ApJ, 878, 132
Pinte, C., Dent, W. R. F., Ménard, F., et al. 2016, ApJ, 816, 25
Pollack, J. B., Hollenbach, D., Beckwith, S., et al. 1994, ApJ, 421, 615
Robitaille, T. P., Whitney, B. A., Indebetouw, R., et al. 2007, ApJS, 169, 328
Shu, F. H., Tremaine, S., Adams, F. C., et al. 1990, ApJ, 358, 495
Sierra, A., Lizano, S., & Barge, P. 2017, ApJ, 850, 115
Sierra, A., Lizano, S., Macías, E., et al. 2019, ApJ, 876, 7
Siess, L., Dufour, E., & Forestini, M. 2000, A&A, 358, 593
Tapia, C., & Lizano, S. 2017, ApJ, 849, 136
van der Marel, N., Dong, R., di Francesco, J., et al. 2019, ApJ, 872, 112
Warren, S. G. 1984, ApOpt, 23, 1206
White, R. J., & Hillenbrand, L. A. 2004, ApJ, 616, 998
Wu, C.-J., Hirano, N., Takakuwa, S., et al. 2018, ApJ, 869, 59
Yang, H., & Li, Z.-Y. 2019, arXiv:1909.08192
Zhang, S., Zhu, Z., Huang, J., et al. 2018, ApJL, 869, L47